Cement and Concrete Research 39 (2009) 548–557

Contents lists available at ScienceDirect

Cement and Concrete Research

journal homepage: http://ees.elsevier.com/CEMCON/default.asp

Short communication

Quantification of tortuosity in hardened cement pastes using synchrotron-based X-ray computed microtomography

M.A.B. Promentilla [a,*], T. Sugiyama [a], T. Hitomi [b], N. Takeda [b]

[a] Environmental Material Engineering Laboratory, Graduate School of Engineering, Hokkaido University, Japan
[b] Technical Research Institute, Obayashi Corp., Japan

ARTICLE INFO

Article history:
Received 19 December 2007
Accepted 3 March 2009

Keywords:
Tortuosity
Microstructure
Cement paste
Synchrotron microtomography
Random walk simulation

ABSTRACT

Tortuosity, as being influenced by the 3D pore micro-geometry, is an important physical quantity to understand better the effect of pore structure on transport properties of cement-based materials. This study attempts to evaluate directly this pore structure-transport parameter from the microtomographic images at spatial resolution of 0.5 μm. This resolution, is by far, to our knowledge, the highest resolution reported for 3D non-invasive imaging of hardened cement pastes. The results show the feasibility of using synchrotron microtomography coupled with 3D image analysis and random walk simulation to measure the diffusion tortuosity that has a direct bearing on transport properties. The tortuosity associated with the percolating pore space seems to reflect the pore morphology that mainly controls the transport properties in young cement pastes; thus, explaining the rough agreement of the results with the computer model or experimental evidence.

1. Introduction

The pore structure of cement-based materials is of primary importance for understanding and modeling the transport phenomena that influences the durability performance of these materials [1,2]. It is well understood that a typical characteristic of any material transport in such complex porous media is that the actual path followed by the transported material is very complicated or tortuous even in the microscopic scale. However, there is still limited information on the nature of connectivity and tortuosity of the pore space in three dimensions. Thus, our study focuses on the three dimensional (3D) micro-geometry of pore structure in hardened cement pastes with the aid of synchrotron-based X-ray computed microtomography.

Among the variety of experimental techniques for pore structure characterization, synchrotron-based microtomography is a viable non-destructive technique that could be employed to examine the 3D microstructure of cement-based materials. It is a 3D imaging technique which is based on the 3D computed reconstruction of a sample from the 2D radiographic projections acquired at different angles around its axis of rotation. In principle, the synchrotron-based microtomography is similar to medical computed axial tomography scans or industrial micro-focus CT; but this technique achieves much higher spatial resolution by combining extremely bright, monochromatic synchrotron radiation with high quality optics and X-ray detection. In addition, reconstruction artifacts such as beam hardening that is commonly encountered in polychromatic CT are also reduced in synchrotron-based microtomography [3].

Synchrotron-based microtomography have been used to porous building materials [4], as well as, to other cementitious materials [5–9] by various researchers in the US and Europe. At SPring-8, a third-generation synchrotron radiation facility in Japan, the pore structure of hardened cement pastes and mortar was also examined at a sub-micron resolution [10,11]. Although this technique has found potential applications in cement and concrete research, evaluation of pore structure tortuosity from such 3D images has not yet been fully explored. In the present communication, we demonstrate the feasibility of evaluating diffusion tortuosity in hardened cement paste by employing 3D-image analysis and random walk simulation to high-resolution microtomographic images obtained at SPring-8, Japan.

2. Background on definition of tortuosity

The concept of tortuosity is typically introduced as some kind of "fudge" factor in macroscopic transport equations to account for the complicated transport paths in porous media. Accordingly, one classic definition of tortuosity (τ) is given as a ratio of 'effective average path', *Le*, of a fluid (or an electric) particle to the corresponding straight and shortest distance, *L*, along the direction of macroscopic flux. In this sense, tortuosity will always be greater than or equal to one. In some literatures, the tortuosity is also defined as the square of this ratio, Le/L. Nevertheless, it is just a matter of definition as it takes

* Corresponding author. Graduate School of Engineering, Hokkaido University, Kita 13 Nishi 8 Kita-ku, Sapporo 060-8628, Japan. Tel./fax: +81 11 706 6178.
E-mail addresses: mabp@eng.hokudai.ac.jp, mpromentilla@gmail.com (M.A.B. Promentilla).

0008-8846/$ – see front matter © 2009 Elsevier Ltd. All rights reserved.
doi:10.1016/j.cemconres.2009.03.005

into account the proper power of this ratio particularly in the forms of the equations used to relate tortuosity to other macroscopic transport properties like permeability and diffusivity. In addition, this definition of tortuosity (Le/L) is not necessarily a property of the porous medium, but a parameter that may be valid only to some geometrical assumptions of the medium such as that of the unidimensional capillary model [12].

In this paper, tortuosity is viewed as a property of the porous medium that can be measured from the 3D micro-geometry of the pore structure. For example, the tortuosity in geologic materials has been estimated based on random walk simulation in the 3D pore space [13,14]. Likewise, this technique allows us to quantify the diffusion tortuosity from high-resolution microtomographic images of cement-based materials [15,16]. Diffusion tortuosity (τ_D) is defined as the ratio of the self-diffusion coefficient (D_o) of non-sorbing walkers in free space to the long-time self-diffusion coefficient (D_∞) of these walkers in pore space. This self-diffusion coefficient of walkers is determined from monitoring the mean square displacement traveled by these walkers as a function of time. The time-dependent diffusion coefficient $D(t)$ associated with the random Brownian motion of molecules can then be used to probe the geometry of porous media [17]. For example, the self-diffusion coefficient of water, measured at long-observation times by NMR diffusometry technique can, in principle, be used to estimate the tortuosity of a porous medium [18,19].

The self-diffusion coefficient of molecules in a bulk medium (free space) is time-independent but becomes time-dependent when measured in a confining geometry (e.g., pore space). At long diffusion time, the self-diffusion coefficient approaches zero in a closed or isolated pore space, but it approaches a limiting non-zero value as diffusing molecules probe the connectivity and tortuosity of an open pore network. In a well-connected pore system, the long-time self-diffusion coefficient of molecule is therefore reduced compared to the one in the bulk medium by the so-called diffusion tortuosity.

Diffusion tortuosity is also related to the accessible porosity (Φ) and the measured electrical tortuosity, also known as, the formation factor (F) such that

$$\frac{D_0}{D_\infty} = \tau_D = F\phi \tag{1}$$

The measured formation factor is the ratio of the electrical conductivity of the electrolyte in the bulk fluid (σ_f) to that of the electrolyte in the porous medium (σ_e) [18]. By Nernst–Einstein relation, the inverse of formation factor is equivalent to the diffusibility or the relative diffusivity (D_e/D_f) of the porous medium where D_e is the measured effective (or intrinsic) diffusion coefficient in terms of the average flux per unit area of the porous medium using Fick's law, and D_f is the diffusion coefficient in the free fluid phase [20,21]. Hence, the porosity, diffusion tortuosity, formation factor and diffusibility are related to each other by the following equation:

$$\frac{\phi}{\tau_D} = \frac{1}{F} = \frac{\sigma_e}{\sigma_f} = \frac{D_e}{D_f} \tag{2}$$

Care must therefore be taken when diffusion tortuosity is used in relation to either formation factor or diffusibility since the term "diffusion coefficient" is defined in two different ways. The self-diffusion coefficient in diffusion tortuosity pertains to self-diffusion process which describes the average distance travelled by the diffusing molecules due to thermal motion in a chemically uniform environment. In contrast, the diffusion coefficient in diffusibility is the diffusion coefficient which describes a diffusion process driven by spatially non-uniform concentration gradient and which goes along with changes in the local concentration of the diffusant.

3. Materials and methods

3.1. Sample preparation and image acquisition

The specimens of hardened cement paste were obtained from ordinary Portland cement (OPC) paste prepared at water to cement ratio of 0.50. A cellulose-based viscosity modifying admixture was also added in the mixture to prevent the segregation. After mixing the cement paste, it was sealed for one day followed by curing in water until the predetermined ages of 2, 7 and 28 days, respectively. Note that these said specimens are hereafter referred to as OPC50-2d, OPC50-7d, and OPC50-28d, respectively. Then, each specimen was crushed and the crushed pieces were soaked with acetone to suspend its hydration. A fragment of about 1 mm at its greatest width and 1 mm in length was prepared from the crushed sample for microtomographic studies.

The X-ray imaging of specimens was performed at the X-ray CT system in SPring-8 (Super Photon ring–8 GeV), Japan. The system consists of an X-ray light source from the beam line, double crystal monochromator, high precision rotation stage, and high resolution X-ray image detector [22]. The transmitted images are detected by X-ray image detector which consists of thin scintillator, optic system and CCD camera. The effective pixel size in the transmitted image is 0.5 μm by 0.5 μm (i.e., the image resolution with an isotropic voxel size of 0.5 μm). In this experiment, the beam energy was set to a value of 15 keV. For each specimen, 1500 X-ray projection images with an angle step of 0.12° and an exposure time of 300 ms each were obtained.

3.2. Extraction of 3D pore space from microtomographic images

First, image normalization or contrast stretching was applied to the whole stack of the reconstructed slices on the basis of the predetermined LAC (linear attenuation coefficient) values of the phases of concern. This procedure allowed us to even out the brightness among the slices and enhance the contrast in the said images. This set of images was also down-sampled from 16-bit to 8-bit grayscale images. Then, SLICE [23], a basic 3D-image analysis program developed in SPring-8, was used for pore segmentation and cluster labeling of the normalized reconstructed grayscale images.

Using simple thresholding, pore segmentation allowed us to separate the pore from the "solid" matrix by defining the range of grayscale value (GSV) associated with pore voxels. The lower bound of GSV associated with pore voxels was set to 0 while the upper bound is set to a pre-defined pore threshold value. It has been shown previously that pore structure parameters derived from microtomographic images are sensitive to pore threshold value [11,24]. Several segmentation routines including the selection of pore threshold value have also been proposed in the literature (e.g., see [5,9,25]). Some researchers define the pore threshold value on the basis of gray level histogram alone while others define the threshold value on the basis of known experimental or theoretical porosity. However, as there is no practical procedure yet to standardize pore segmentation, which method is appropriate is still an open discussion.

In this study, two procedures of pore segmentation were used and both are referred here as Method 1 and Method 2, respectively. Method 1 defines the pore threshold value on the basis of transition point in segmented porosity–threshold dependency curve described in Ref. [24]. At this transition point, it is assumed that the segmented porosity started to increase rapidly such that the boundary between pore and the solid matrix is most likely to be segmented as pore space. On the other hand, Method 2 defines the pore threshold value that would match the porosity derived from simple thresholding to either experimental or theoretical porosity value.

After pore segmentation, pore connectivity analysis was then performed using cluster multiple labeling technique as commonly

described in percolation theory [26–28]. In this analysis, pore voxels are considered connected to form a "cluster" when the said voxels are orthogonally in face-to-face contact to each other. In other words, the two voxels are connected to each other when both share a common face. This cluster multiple labeling procedure allowed us then to identify and extract the largest percolating pore cluster if any from the other smaller isolated or dead-end pore clusters. In addition, the degree of pore connectivity was evaluated by determining the fraction of the segmented porosity that forms the largest pore cluster and percolates along the three orthogonal directions (x, y and z-axis). Thus, a pore connectivity of zero indicates that depercolation occurs in at least one of the orthogonal directions, whereas a pore connectivity of one indicates that all pore voxels in the segmented porosity are interconnected to each other.

3.3. Quantification of tortuosity from random walk simulation in 3D pore space

A 3D random walk technique [14] implemented in Mathematica was employed to compute the mean-square displacement of random walkers in the percolating pore space of a simple cubic lattice. Mirror image boundary conditions were applied on the original 3D image of cubic lattice (L^3), resulting to an expanded $(3L)^3$ system where simulations are performed. In this random walk simulation, the walker migrates on a pore voxel chosen randomly as the start position of the lattice walk trial at integer time equals to 0. A trial move is performed with the space step of one unit in one of the six possible directions. The walker then executes a random jump to one of the nearest pore voxels and the time of lattice walk is incremented by a unit integer time after the jump. If the randomly selected voxel is a solid voxel, the jump is not performed but the time is still incremented by one unit. This portrays the restricted motion analogous to that of the 'blind ant trying to escape in the labyrinth' to simulate the diffusion of a particle in a disordered media [27].

Prior to application of the method to the complex pore space of hardened cement paste, we have confirmed that, for a simple capillary model, the random walk technique yields values of diffusion tortuosity that are in agreement with the classic definition of tortuosity factor (i.e., $(Le/L)^2$). Fig. 1 describes the trajectory of a walker in cubic lattice and the computed mean square displacement (MSD) of such trajectories averaged over a number of walkers. In this case, the central subset (10^3 voxels) of the mirror-operated lattice (30^3 voxels) was the 3D image of free space (i.e., all voxels are referred to pore space). In contrast, Fig. 2 describes the output of random walk simulations in confined pore spaces as represented by three simple capillary tube models that percolate in x-direction only. Note that the self-diffusion

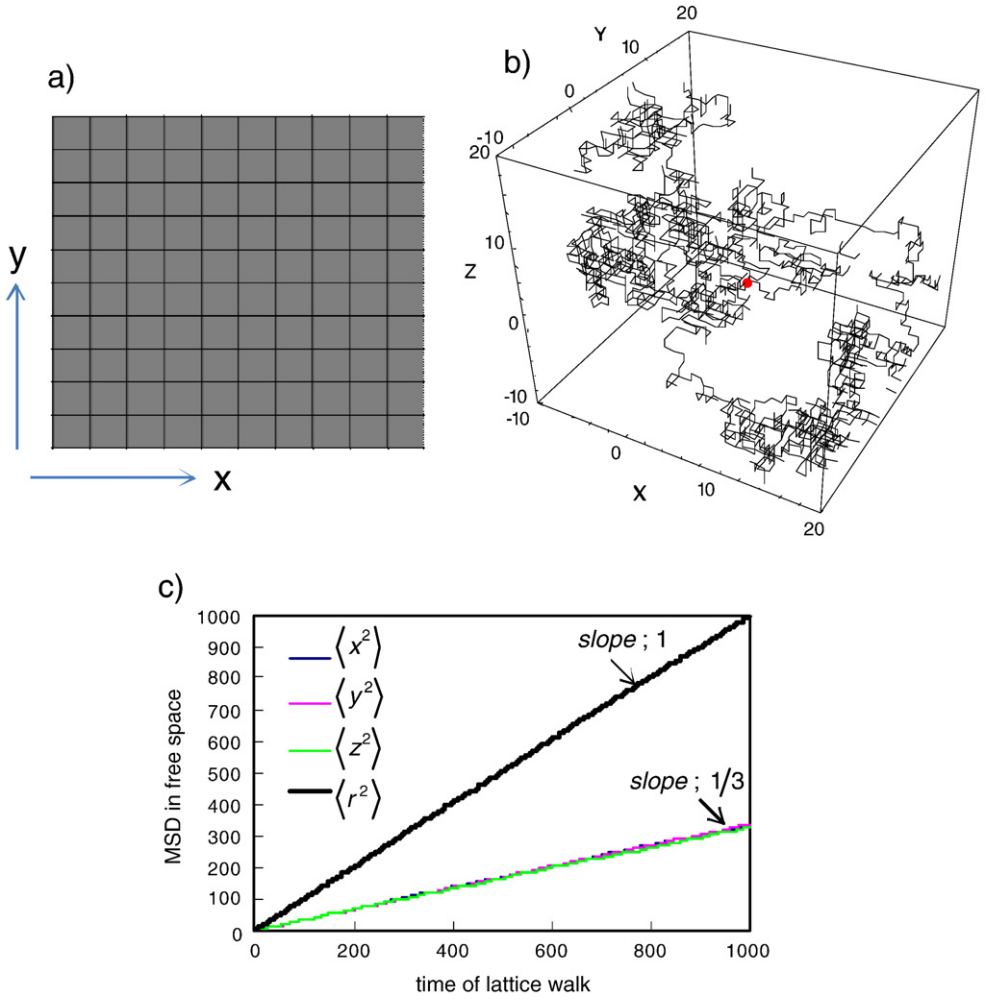

Fig. 1. 3D random walk simulation in a cubic lattice with mirror image boundary conditions. (a) 10×10 voxels of slice image (pore voxels are gray) representing free space (10^3 voxels). (b) 3D view of the trajectory of a walker in a mirror-operated lattice (30^3 voxels). (c) Plot of dimensionless mean square displacement (MSD) vs. time in 3D ($\langle r^2 \rangle$) and in each orthogonal direction. The quantities, $\langle x^2 \rangle$, $\langle y^2 \rangle$, and $\langle z^2 \rangle$ in free space are nearly the same, yielding a common slope of about 1/3 whereas the slope of $\langle r^2 \rangle$ vs. time is about one.

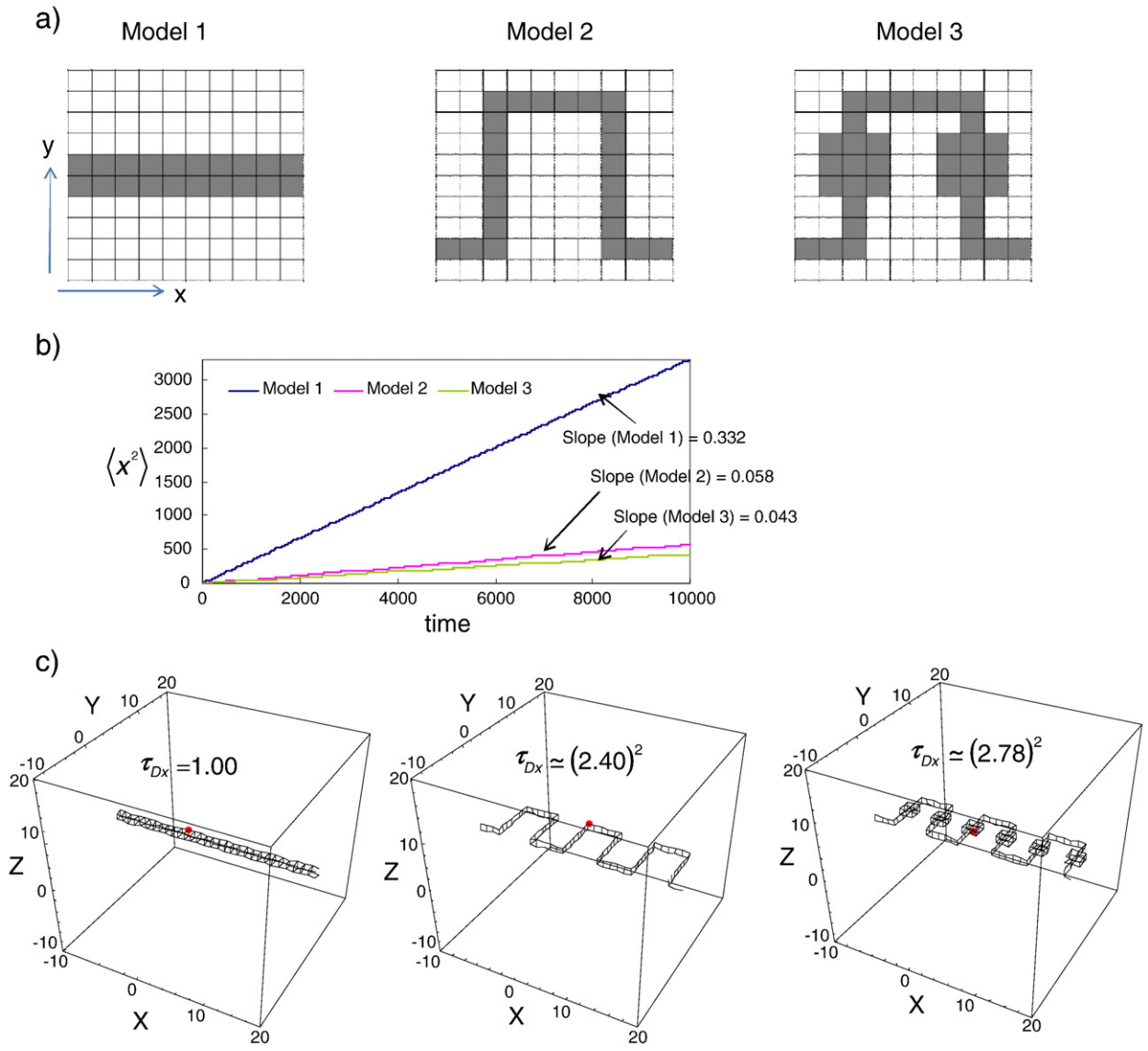

Fig. 2. Random walk simulations in pore space represented by three simple capillary tube models. (a) 10×10 voxels image (gray and white voxels are pore and solid voxels, respectively) of three simple models of tube percolating in x-direction only. (b) Plot of $\langle x^2 \rangle$ vs. time and the computed slope for each model. (c) Sample trajectory of a walker in the percolating pore space. The directional diffusion tortuosity (τ_{Dx}) along the x-axis for each model is calculated by Eq. (5b).

coefficient (D_∞) can be calculated from the limiting slope of the mean square displacement ($\langle r^2 \rangle$) averaged over n walkers against time (t) such that [11,14,29]:

$$D_\infty = \frac{1}{6}\lim_{t\to\infty}\frac{\mathrm{d}\langle r^2(t)\rangle}{\mathrm{d}t} \tag{3a}$$

where

$$\langle r^2(t)\rangle = \frac{1}{n}\sum_{i=1}^{n}\left[(x_i(t)-x_i(0))^2 + (y_i(t)-y_i(0))^2 + (z_i(t)-z_i(0))^2\right] \tag{3b}$$

Likewise, the directional self-diffusion coefficient can also be calculated using the mean square displacements for each orthogonal direction (e.g., the x-axis) such that

$$D_{xx} = \frac{1}{2}\lim_{t\to\infty}\frac{\mathrm{d}\langle x^2(t)\rangle}{\mathrm{d}t} \tag{4a}$$

where

$$\langle x^2(t)\rangle = \frac{1}{n}\sum_{i=1}^{n}\left[(x_i(t)-x_i(0))^2\right] \tag{4b}$$

Thus, the self-diffusion coefficient of walkers in free space (i.e., D_o) was computed to be 1/6 as the slope ($\langle r^2 \rangle$ vs. t) shown in Fig. 1c is nearly equal to 1.0. This is the expected value since the simulation in the cubic lattice uses a lattice constant of unity. The average diffusion tortuosity and directional diffusion tortuosity (e.g., in x-direction) can therefore be estimated from the following equations:

$$\tau_D = \left[\lim_{t\to\infty}\frac{\mathrm{d}\langle r^2(t)\rangle}{\mathrm{d}t}\right]^{-1} \tag{5a}$$

$$\tau_{Dx} = \left[3\left\{\lim_{t\to\infty}\frac{\mathrm{d}\langle x^2(t)\rangle}{\mathrm{d}t}\right\}\right]^{-1} \tag{5b}$$

Since the pore space in Fig. 2 is percolating in the *x*-direction only, the time-derivative of the directional mean-square displacement of walkers in the y and z directions are expected to approach zero as its limiting value. In this case, it would be meaningful to estimate the directional tortuosity of the pore space along the *x*-axis only. Using Eq. (5b), the directional tortuosity is therefore obtained from the reciprocal of thrice the slope shown in Fig. 2b. For example, the diffusion tortuosity (τ_{Dx}) in the *x*-direction for the straight (Model 1) and tortuous tube (Model 2) were computed to be equal to 1.0 (or 1.0^2) and 5.76 (or 2.40^2), respectively. This computed diffusion tortuosity in the *x*-direction was found to be consistent with the geometric tortuosity attributed to degree of tube elongation (see Fig. 2a) defined as $(Le/L)^2$. Interestingly, a higher value of diffusion tortuosity (2.78^2) was also observed for the same tortuous pipe but with varying cross section. This implies that the diffusion tortuosity is influenced by the geometric details of the pore structure that includes pore constrictions and nonuniform cross-sectional area of pores. Since a more realistic 3D pore space can be extracted directly from microtomographic images, the diffusion tortuosity is a key pore structure-transport parameter to describe restricted diffusion as being influenced by the complex pore geometry in hardened cement pastes.

4. Results and discussion

4.1. Pore structure parameter from microtomographic images

For the purpose of illustration, a region of interest (ROI) was selected of which a cubic volume of interest (VOI) was obtained from the original data set of each specimen. In this study, the VOI was limited to 450^3 voxels (225^3 μm^3), avoiding the possible selection of surrounding air and edge effects in the ROI, as well as, reducing the computational resource required for image analysis and computer simulation. An example of the results from image analysis of the VOI is shown in Fig. 3. The segmented porosity refers to the extracted pore

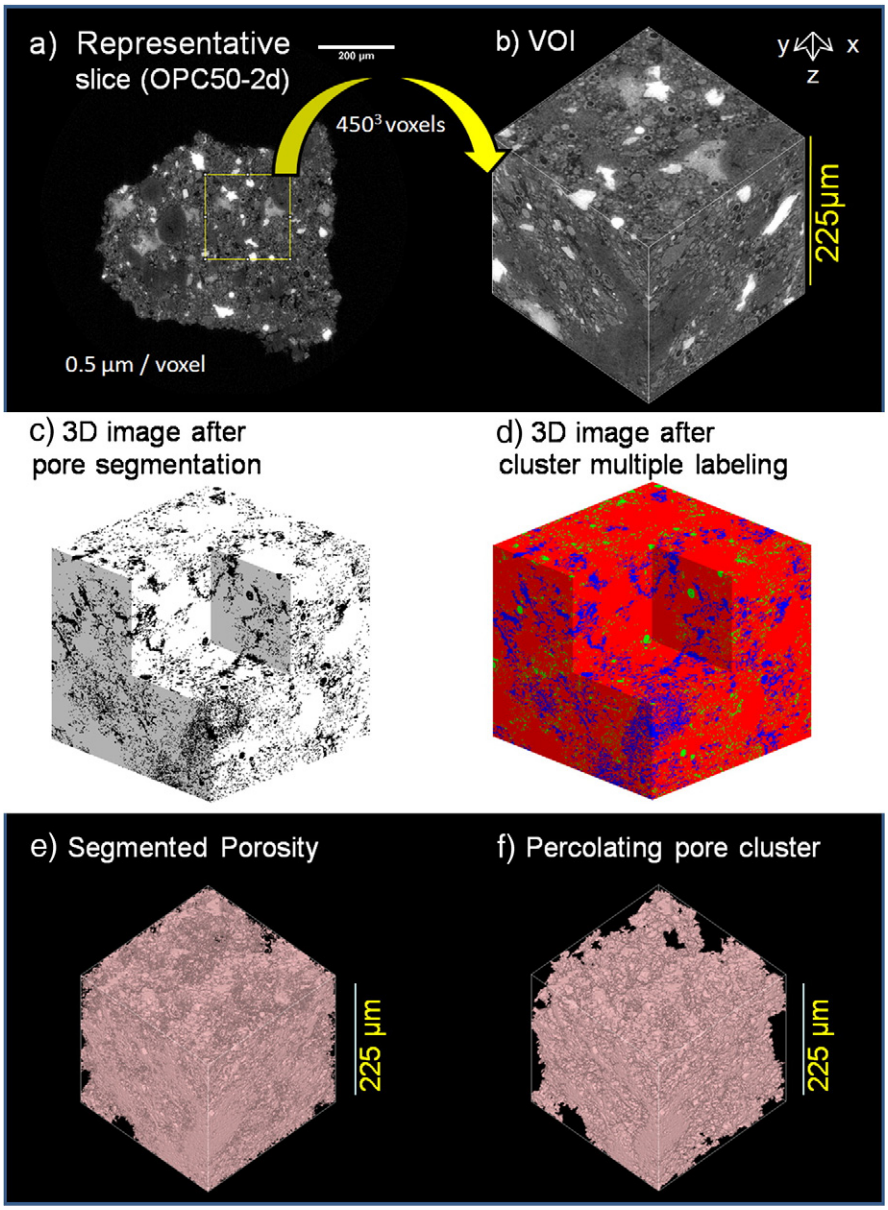

Fig. 3. Extraction and visualization of pore space from microtomographic images. (a) An 8-bit grayscale image of the representative slice (2000 × 2000 voxels) of OPC50-2d. (b) The volume of interest (VOI = 450^3 voxels or 225^3 μm^3) extracted from the original data set. (c) Stacking up of binary images after pore segmentation of the VOI. The pore and solid voxels are imaged as black and white, respectively. (d) Cluster multiple labeling of image in (c) resulting a 3D image wherein the solid voxels are imaged as red and the largest percolating pore cluster is imaged as blue. The dead-end pore and isolated pore clusters in the VOI are imaged as green. Volume rendering of the pore voxels (color shaded) in the segmented porosity and percolating pore cluster are also shown in (e) and (f), respectively.

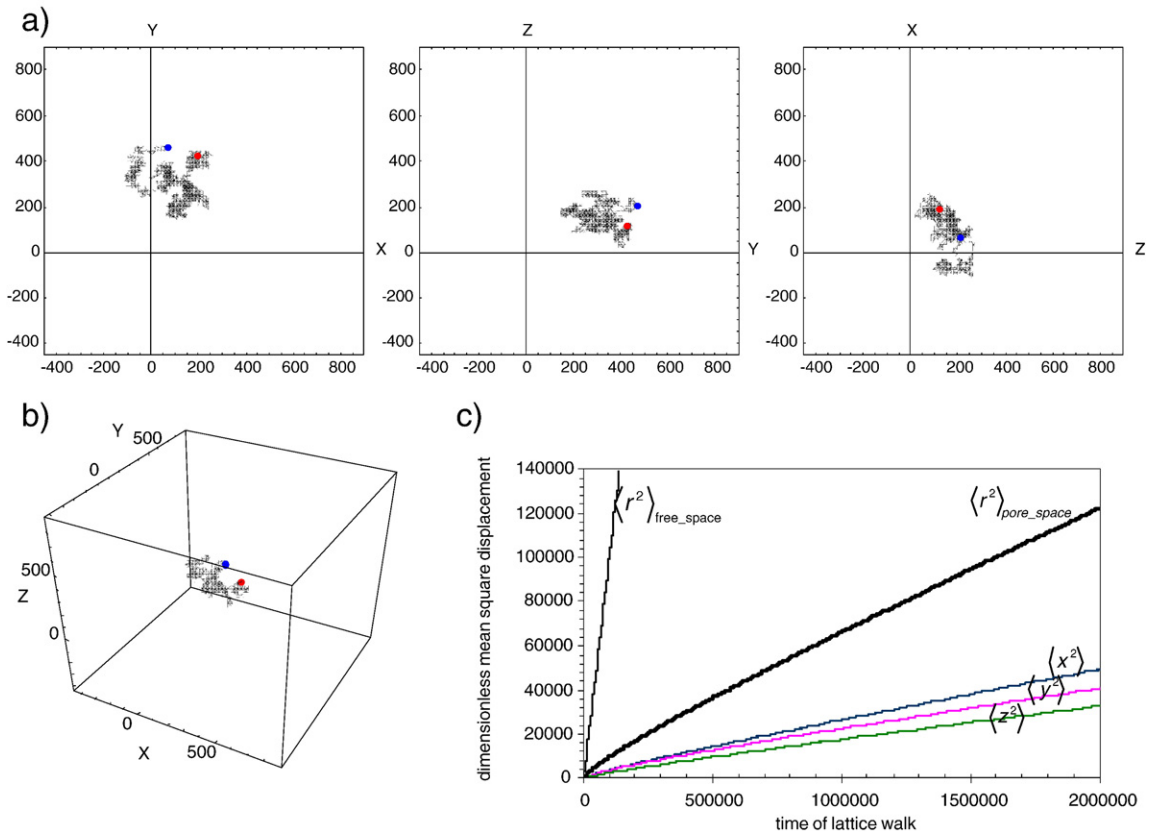

Fig. 4. Examples of output from the 3D random walk simulation in the percolating pore space of OPC50-2d. (a) Projected trajectory of a walker in the three orthogonal planes. (b) The 3D view of the trajectory wherein the total time step is 2 million. c) Plot of dimensionless mean square displacement ($\langle r^2 \rangle$) vs. time of 50,000 walkers for both free space and percolating pore space. The mean square displacements ($\langle x^2 \rangle$, $\langle y^2 \rangle$, and $\langle z^2 \rangle$) in the three orthogonal directions for percolating pore space of OPC50-2d are also shown.

space after segmentation whereas the percolating pore cluster is the largest pore cluster that percolates in three orthogonal directions. Furthermore, this percolating pore cluster is also referred here as the effective porosity since this open and interconnected part of the segmented porosity would most likely contribute to the long-distance material transport in cement pastes.

Fig. 4 describes an example of output from 3D random walk simulation in the percolating pore space. Random walk simulation in free space (i.e., 100% porosity) of the same VOI size was also performed, and as expected, yielded a diffusion tortuosity of one. As shown in Fig. 4c, the dimensionless mean-square displacement (MSD) averaged over 50,000 walkers is plotted against the dimensionless time (maximum time step $= 2 \times 10^6$) of lattice walk. The curve of MSD against time in pore space indicated the restricted diffusion which resulted to a reduced self-diffusion coefficient of the walkers relative to the one in free space (unconstrained diffusion). Here, the limiting slope of MSD against time corresponds to the inverse of average tortuosity (or normalized self-diffusion coefficient, $D_{\text{porespace}}/D_{\text{freespace}}$) in 3D pore space. Likewise, the limiting slope of MSD in each orthogonal direction against time corresponds to one third of the inverse of directional tortuosity. The harmonic mean of these three orthogonal directional tortuosities is equivalent to the average diffusion tortuosity.

Table 1 summarizes the pore structure parameters derive from the microtomographic images of hardened cement pastes ($w/c = 0.50$) of curing age of 2 days (OPC50-2d), 7 days (OPC50-7d) and 28 days (OPC50-28d), respectively. Note that the two methods namely Method 1 and Method 2 differ on how the pores were extracted in particular to the choice of pore segmentation threshold value. As Method 1 depends solely on the gray level histogram, selection of its pore threshold value does not require any prior information of the experimental or theoretical porosity. As for Method 2, we used a pore threshold value to correspond the segmented porosity to the value of the theoretical capillary porosity.

The theoretical capillary porosity (Φ_{cap}) was estimated from the Powers model [30], where $\Phi_{\text{cap}} = (w/c - 0.36\alpha)/(w/c + 0.32)$. The degree of hydration (α) was assumed based on the evaluated volume fraction of unreacted cement particles in the microtomographic images. Then, using a water to cement ratio (w/c) of 0.50, the predicted theoretical capillary porosity of OPC50-2d, OPC50-7d, and OPC50-28d were computed to be about 0.40, 0.34, and 0.31, respectively.

It is not surprising that the segmented porosity obtained from Method 1 is lower than the theoretical porosity value, considering the results from image analysis depend strongly on pore threshold value and the resolution of digitized image. Given the current image

Table 1
The pore structure parameters derived from microtomographic images.

Pore structure parameters	Method 1			Method 2		
	OPC50-2d	OPC50-7d	OPC50-28d	OPC50-2d	OPC50-7d	OPC50-28d
Segmented porosity	0.18	0.15	0.14	0.40	0.34	0.31
Pore connectivity	0.82	0.75	0.59	0.98	0.97	0.94
Effective porosity	0.15	0.12	0.09	0.39	0.33	0.29
Diffusion tortuosity (x, y, z)[a]	18 (14.9, 18.5, 22.1)	26 (22.3, 23.6, 35.8)	118 (97.2,107.3, 168.7)	3 (3.1, 3.1, 4.2)	5 (4.1, 3.9, 5.9)	9 (8.4, 7.0, 11.3)
Formation factor	122	223	1386	9	14	29

[a] The values enclosed in the parenthesis are the directional tortuosities along the x, y and z-axis.

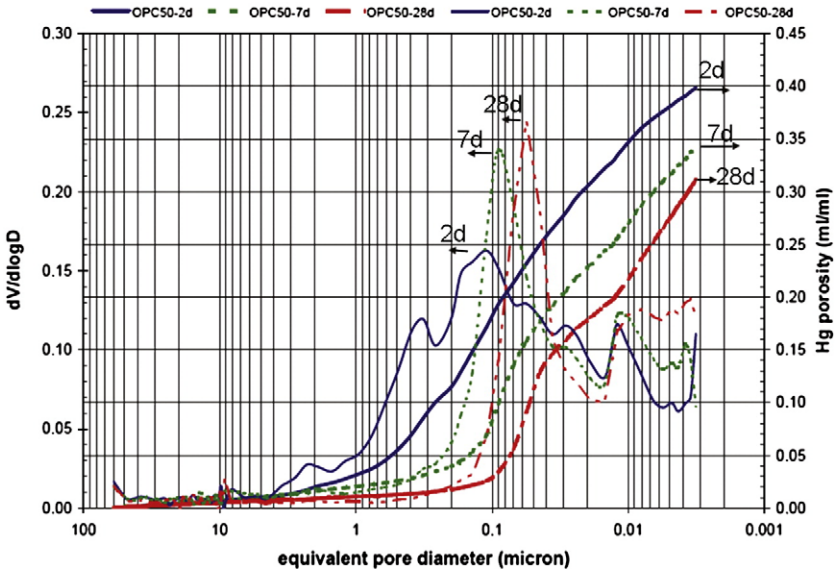

Fig. 5. Pore structure characterization of each specimen using mercury intrusion porosimetry (MIP).

resolution (0.5 μm/voxel), the pores of size smaller than 0.5 μm may not be resolved properly in the microtomographic images, resulting to the exclusion of some of these fine pores in the segmented porosity of Method 1. On one hand, the theoretical porosity according to Powers model includes pore sizes down to few nanometer scales. For this reason, the segmented porosity obtained from Method 2 may have included unexpectedly the finer pores that are attributed to partial volume effects [11,31] in microtomographic images.

It is also instructive to compare the porosity derived from image analysis with other experimental techniques. For example, the mercury intrusion porosimetry (MIP), a commonly used technique for pore size studies, was employed to measure the experimental porosity of the specimens that were prepared from the same batch mix of OPC50-2d, OPC50-7d and OPC50-28d. As shown in Fig. 5, the Hg-accessible porosity of OPC50-2d, OPC50-7d and OPC50-28d were found coincidentally to be nearly the same value of the theoretical porosity derived from Powers model. Note that the Powers model and Hg-accessible porosity describe two different definition of porosity in hardened cement pastes. The porosity from MIP does not include isolated voids whereas the segmented porosity from image analysis accounts all capillary pores regardless of their connectivity. In addition, the MIP technique covers a wider range of pore sizes (i.e., between 3 nm to 60 μm) as compared to the range of pore size that can be detected and resolved properly through microtomography.

As cement pastes include gel pores, capillary pores, hollow shell pores, and large air voids, it is quite difficult to characterize fully the pore structure because its pore sizes extend over a wide range of length scale. As certain technique would apply only on a certain range of pore sizes, different techniques may yield different values for the same pore structure parameters (e.g., porosity). Caution must also be exercised in comparing values from different techniques as interpretation of the results depends on some underlying assumptions. For example, MIP is an invasive and indirect method that makes assumptions about the pore geometry to analyze experimental data. On one hand, synchrotron microtomography is a non-invasive and direct method to examine capillary pores at a spatial resolution down to submicron scale. Accordingly, the lower end of the pore size range that can be detected in principle from microtomography is determined by its spatial resolution whereas the upper end can be as large as possible depending on the specimen size. In spite of its limited range of pore size when compared to other indirect techniques, synchrotron microtomography is, to date, the most viable noninvasive and nondestructive imaging technique that can provide directly the 3D information of the pore network that are more relevant to transport properties of hardened cement pastes [5,7,11]. This technique could therefore complement the other techniques such as that of MIP in studying microstructure-property relationship.

4.2. Comparison with NIST computer model

In recent years, computer-aided microstructure models have also been successfully applied to predict the transport properties of hardened cement pastes. For example, the NIST microstructure model has been used to predict the relative diffusivity (or inverse of formation factor) of cement pastes on the basis of the capillary porosity obtained from 3D image-based cement hydration model [21,32,33]. Given the segmented porosity, we compared the predicted values from NIST model to the measured formation factors obtained from microtomographic images (see Fig. 6). These measured formation factors from the images were evaluated by normalizing the tortuosity values derived from random walk simulation with their corresponding effective porosity (see Table 1). Although this study is limited in its extent, a relatively good consistency is found between the values predicted from the NIST model and the measured formation factor, particularly for images wherein the segmented porosity is much farther away from the predicted percolation threshold. From NIST model simulations, this percolation threshold ($\Phi_{cap} = 0.18 \pm 0.05$) is the porosity where the capillary pores become disconnected, resulting to an overall diffusivity being controlled by the diffusivity of CSH paste [32,33]. However, there

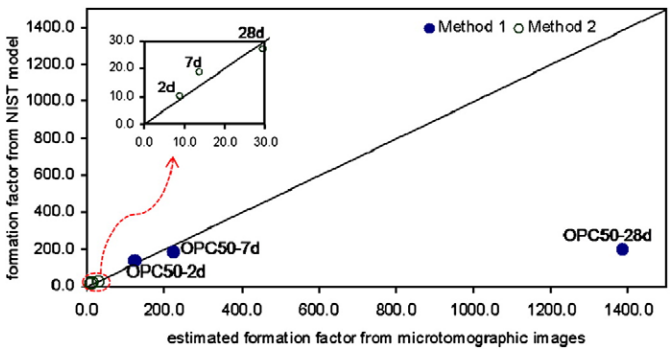

Fig. 6. Comparison between the formation factor obtained from NIST model [32–33] and that obtained from microtomographic images.

is no consensus yet on the value of porosity where actual depercolation can physically occur for a given cement paste [34].

4.3. Percolation of segmented porosity

In any case, as the capillary porosity increases and becomes farther away from its percolation point, the measured tortuosity or formation factor decreases because the pore space are better connected to each other. Thus, the pore morphology in segmented porosity, particularly its pore connectivity, will directly influence the reliability of the computed tortuosity from microtomographic images. Fig. 7 describes the relationship between the segmented porosity and pore connectivity in the considered VOI (volume of interest) of each specimen. As pore connectivity approaches to zero (i.e., near depercolation), fewer and fewer pores of the segmented porosity are interconnected to form percolation. Notable differences in the pore connectivity at a given porosity among specimens could reveal significant differences in their pore morphology. For example, the degree of pore connectivity of OPC50-28d appeared to be much lower than that of OPC50-2d or OPC50-7d. This may also suggest that pores from the images are becoming more difficult to resolve by synchrotron microtomography because of the increased presence of finer pores at longer curing time.

Nevertheless, the results seem reasonable and the trend appears to be consistent with percolation studies of capillary porosity from various computer models with digital resolutions comparable to that of microtomographic images [33–35]. Our preliminary finding also shows rough agreement with that of the microtomographic studies reported in Ref. [7]. Given the spatial resolution of 0.7-μm, Gallucci et al. observe that the total porosity of a 1-day old hardened cement paste ($w/c = 0.50$) drops from about 0.16 to near zero after 28 days of curing; and also, the pore network does not percolate any longer after 7 days. On the other hand, our results (see Table 1) showed percolation of pore space even for hardened cement pastes of 28 days of curing (OPC50-28d), although with a much lower degree of pore connectivity as compared with that of OPC50-2d and OPC50-7d.

4.4. Pore anisotropy and porosity–tortuosity relationship

From the microtomographic images, we also examined the pore anisotropy for the tortuosities measured along the three orthogonal directions. Fig. 8 illustrates these computed tortuosities derived from 8 independent subvolumes (225^3 voxels) of the original VOI (450^3 voxels) in each specimen. Results indicate larger tortuosities and more pronounced pore anisotropy was observed for Method 1 as compared with that of Method 2. Such difference may be attributed to denser interconnectivity of pores that were obtained from Method 2. Likewise, the more pronounced pore anisotropy exhibited by OPC50-28d as compared with that of OPC50-2d and OPC50-7d suggests poor interconnectivity of pores at longer curing time.

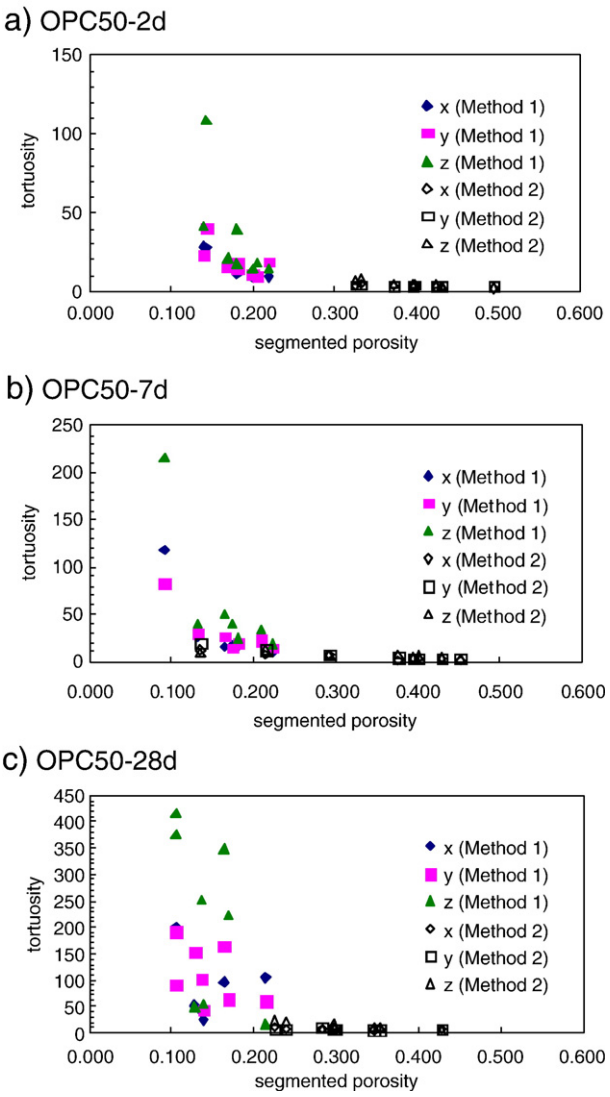

Fig. 8. Plots of directional tortuosity (x, y and z-directions) vs. segmented porosity in 8 independent subvolumes (VOI = 225^3 voxels) of the original VOI (450^3 voxels).

Interestingly, from a large ensemble of subvolumes of a single volumetric data set, properties of porous materials can be evaluated over a wider range of porosities to describe the microstructure-property relationship [36,37]. In Fig. 9, we plot the average tortuosity normalized by the effective porosity as a function of segmented porosity regardless of the age of the hardened cement pastes. In this figure,

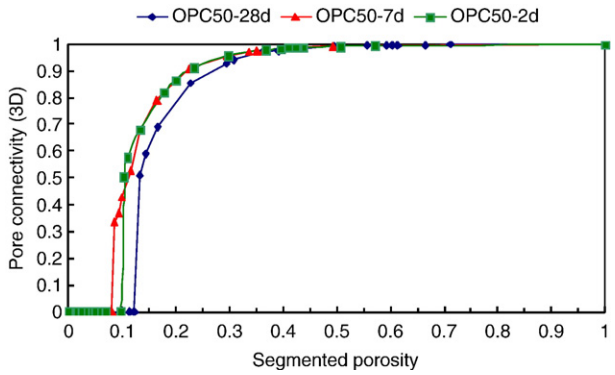

Fig. 7. Degree of pore connectivity vs. the segmented porosity in the considered VOI of the microtomographic images for each specimen.

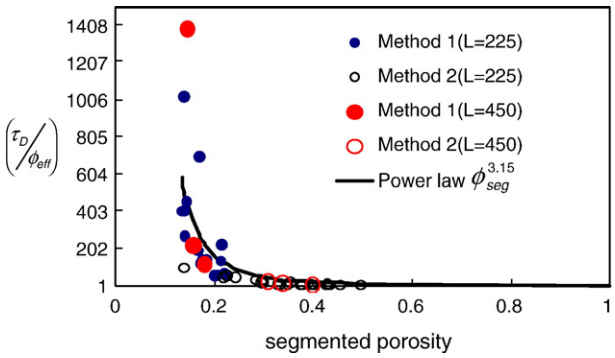

Fig. 9. Plot of evaluated formation factor vs. segmented porosity from the analysis of microtomographic images.

an empirical fit in the form of power function was shown using a fitting parameter of 3.15 that was obtained from nonlinear regression analysis. Clearly, the plot suggests strong correlation between the computed formation factor (τ_D/ϕ_e) and segmented porosity at porosity above 0.20, whereas more scattering of data was observed at porosity below this value. In addition, as the porosity crosses the value of about 0.20, the plot exhibited a significant and sudden increase of tortuosity. This seems to be consistent with the experimental results of Powers et al. [38] on water permeability measurements. They suggest that the capillary pores in cement pastes exhibit a percolation transition from connected to disconnected phase at a porosity of about 0.20, wherein a sharp decrease of permeability is observed.

4.5. Influence of digital resolution

As is the case of any digital image-based techniques, the pore structure parameters derived from synchrotron microtomography are influenced by digital resolution. It has been shown from either microstructure models [33–35] or microtomographic studies [7] that increasing the pixel (or voxel) size decreases the computed pore connectivity. Fig. 10 illustrates the effect of increasing the voxel size (i.e., digital resolution of the microtomographic images) on the segmented porosity and pore connectivity in the considered VOI of OPC50-2d. We binned the voxels of cluster of sizes N^3 ($N=2$, 3, and 4) to their average value to generate the images at coarser resolution, resulting to realizations of the original microtomographic images at integers multiple of the voxel size of the original image (i.e., $N\times 0.5\ \mu m = 1.0\ \mu m$, 1.5 μm, and 2.0 μm). We then used the pore threshold values that were originally used in Method 1. As expected, the segmented porosity goes down as the image resolution becomes coarser (i.e., the voxel size increases). Clearly, this influences the evaluation of pore connectivity as shown in Fig. 10e. At coarser resolution, the diffusion tortuosity will essentially be higher as the degree of pore connectivity becomes lower. For example, the computed diffusion tortuosity for OPC50-2d increased from 18 to 46 when the voxel size increased from 0.5 μm to 1.0 μm. Note that at coarser resolution (≥1.0 μm/voxel), the pore space in OPC50-28d was no longer percolating in three orthogonal directions.

In the discussion above, some open issues may still remain on whether the scale at the current resolution of synchrotron microtomography could measure the pore structure parameters relevant to the transport properties of hardened cement pastes. If one would argue that MIP is adequate enough to characterize pore structure in hardened cement pastes, then the critical pore diameter is said to be the length scale that plays an important role in the transport properties [39–41]. This parameter corresponds to the diameter of the smallest pore of the set of largest pores that percolate through the material. In mature cement pastes, this critical pore size obtained from MIP could range between 20 nm and 100 nm, and such length scale may not be resolved properly from the current spatial resolution of the method.

Nevertheless, the diffusion tortuosity derived from the digitized images seems to reflect the pore morphology that mainly controls the transport properties in young cement pastes; thus, explaining the rough agreement with the computer model or experimental evidence. Moreover, it has also been shown that water vapor diffusivity and water permeability through hardened cement pastes can be reasonably estimated from a pore network model extracted from microtomographic images because of the self-similarity of the capillary pore space [25]. Due to such pore space fractality, it is assumed that the images could provide the same pore space morphology with that of the actual transport-relevant part of hardened cement pastes. Thus, synchrotron microtomography can be a valuable technique to provide qualitative and quantitative information of the 3D micro-geometry and morphology of pore structure without resorting to any assumption of pore geometry. As the X-ray imaging system continues to improve for higher spatial resolution, this technique can therefore contribute significantly to the investigation of microstructure-property relationship in cementitious materials.

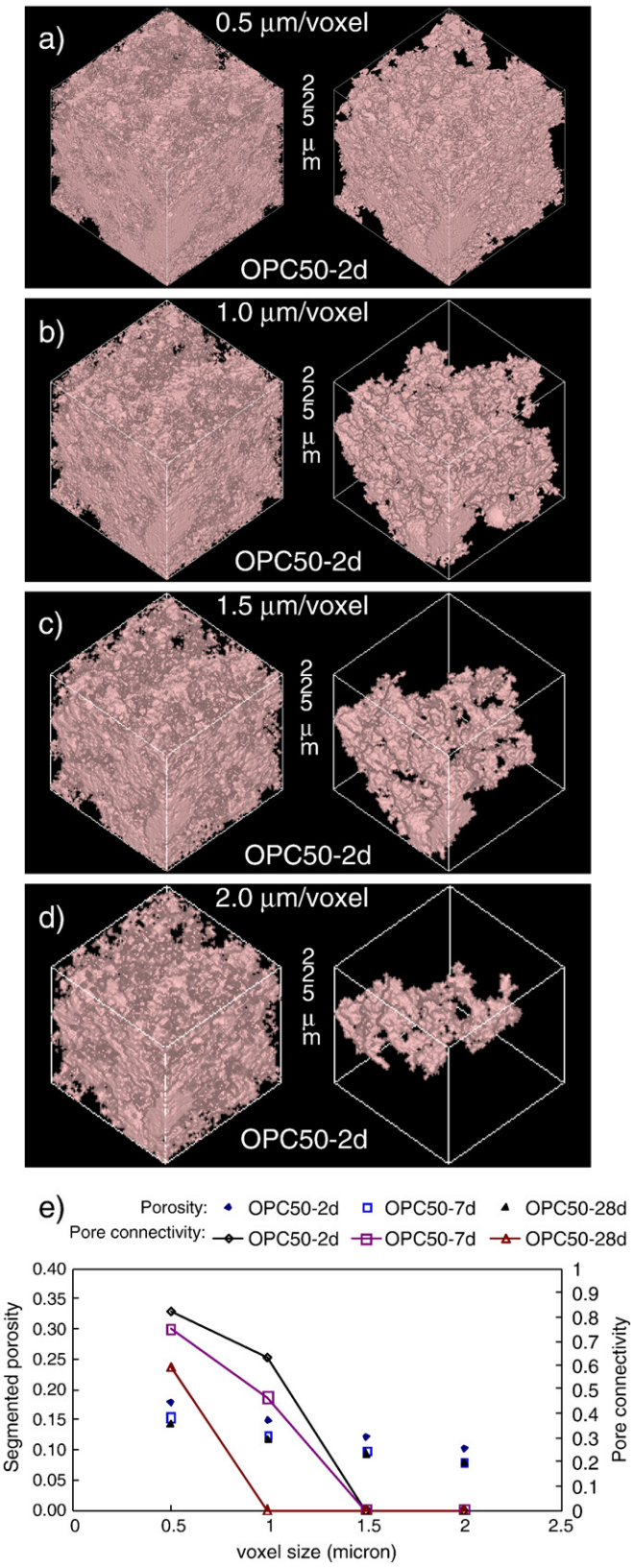

Fig. 10. Influence of digital resolution on the porosity and pore connectivity. Figures in (a) to (d) are the segmented porosity (left) and the corresponding largest pore cluster (right) of OPC50-2d at different voxel size. (e) Plot of segmented porosity and pore connectivity vs. voxel size (or digital resolution).

5. Conclusion

Using synchrotron microtomography, the 3D micro-geometry of hardened cement paste of different ages (2, 7, 28 days) was examined from images of very high spatial resolution (0.5 μm/voxel) obtained at SPring-8, Japan. Diffusion tortuosity in the largest percolating pore cluster was then quantified using 3D-image analysis and random walk simulation. As the age of hardened cement paste increases, results indicate that the tortuosity increases while the percolating effective porosity decreases as the pores that can be resolved at the given resolution becomes fewer and fewer, and more disconnected. Although the resolution may still be insufficient to resolve the finer pores, the non-invasive 3D imaging of the pore space allows us to investigate the pore connectivity and tortuosity which is difficult if not impossible to obtain using 2D microscopic imaging alone or other indirect techniques. This is one of the most important advantages of using 3D micro-geometry technique since it provides information that could complement with the other experimental analyses as regard to pore structure characterization of hardened cement pastes. Furthermore, the synchrotron microtomography is expected to be a powerful tool in the study of pore structure-transport property of hardened cement paste as the X-ray CT system continues to improve for higher spatial resolution. Future research would therefore involve investigations on the robustness of the method particularly in its application to predict the transport properties of cement-based material on the basis of the measured pore structure parameters from the microtomographic images.

Acknowledgments

Part of this present research work was funded by the Japan Society for the Promotion of Science (Research No.: 1965610607, A representative: Takafumi Sugiyama) and the Center of Excellence (COE) program in Graduate School of Engineering at Hokkaido University. The authors would like to thank them for their financial support. The synchrotron radiation experiments were performed at the BL20XU in SPring-8 with the approval of the Japan Synchrotron Radiation Research Institute (JASRI) (Proposal No. 2007A1951-NL-np).

References

[1] T. Sugiyama, W. Ritthichauy, Y. Tsuji, Simultaneous transport of chloride and calcium ions in hydrated cement systems, J. Adv. Concr. Technol. 1 (2) (2003) 127–138.
[2] T. Sugiyama, W. Ritthichauy, Y. Tsuji, Experimental investigation and numerical modeling of chloride penetration and calcium dissolution in saturated concrete, Cem. Concr. Res. 38 (2008) 49–67.
[3] D. Ashbridge, M. Thorne, M. Rivers, J. Muccino, P.A. O'Day, Image optimization and analysis of synchrotron X-ray computed microtomography data, Comput. Geosci. 29 (2003) 823–836.
[4] D.P. Bentz, D.A. Quenard, H.M. Kunzel, J. Baruchel, F. Peyrin, N.S. Martys, E.J. Garboczi, Microstructure and transport properties of porous building materials. II: three-dimensional X-ray tomographic studies, Mat. Struct. 33 (2000) 147–153.
[5] D.P. Bentz, S. Mizell, S. Satterfield, J. Devaney, W. George, P. Ketcham, J. Graham, J. Porterfield, D. Quenard, F. Vallee, H. Sallee, E. Boller, J. Baruchel, The visible cement data set, J. Res. Natl. Inst. Stand. Technol. 107 (2002) 137–148.
[6] N. Burlion, D. Bernard, Da Chen, X-ray microtomography: application to microstructure analysis of a cementitious material during leaching process, Cem. Concr. Res. 36 (2006) 346–357.
[7] E. Gallucci, K. Scrivener, A. Groso, M. Stampanoni, G. Margaritondo, 3D experimental investigation of the microstructure of cement pastes using synchrotron X-ray microtomography, Cem. Concr. Res. 37 (2007) 360–368.
[8] L. Helfen, F. Dehn, P. Mikulik, T. Baumbach, Three-dimensional imaging of cement microstructure evolution during hydration, Adv. Cem. Res 17 (3) (2007) 103–111.
[9] S. Lu, E.N. Landis, D.T. Keane, X-ray microtomographic studies of pore structure and permeability in Portland cement concrete, Mat. Struct. 36 (2006) 11–20.
[10] T. Hitomi, Y. Mita, H. Saito, N. Takeda, Observation of fine structure of mortar using X-ray CT images at SPring-8, Proceedings of Annual Conference of Japan Concrete Institute, vol. 26 (1), 2004, pp. 645–650, in Japanese.
[11] M.A.B. Promentilla, T. Sugiyama, T. Hitomi, N. Takeda, Characterizing the 3D pore structure of hardened cement paste with synchrotron microtomography, J. Adv. Concr. Technol. 6 (2) (2008) 273–286 (Japan Concrete Institute).
[12] P. Grathwohl, Diffusion in Natural Porous Media: Contaminant Transport, Sorption/Desorption and Dissolution Kinetics, Kluwer Academic Publishing, Boston, 1998.
[13] Y. Nakashima, T. Nakano, K. Nakamura, K. Uesugi, A. Tsuchiyama, S. Ikeda, Three-dimensional diffusion of non-sorbing species in porous sandstone: computer simulation based on X-ray microtomography using synchrotron radiation, J. Contam. Hydrol. 74 (2004) 253–264.
[14] Y. Nakashima, S. Kamiya, Mathematica programs for the analysis of three-dimensional pore connectivity and anisotropic tortuosity of porous rocks using X-ray microtomography, J. Nucl. Sci. Technol. 44 (9) (2007) 1233–1247.
[15] M.A.B. Promentilla, T. Sugiyama, Studies on 3D micro-geometry and diffusion tortuosity of cement-based materials using X-ray microtomography, Proceedings of the 32nd Conference on Our World in Concrete and Structures, Singapore, Aug. 2007, pp. 389–396.
[16] M.A.B. Promentilla, T. Sugiyama, Evaluation of tortuosity of cement-based materials with X-ray synchrotron radiation microtomography, Proceedings of the 1st International Conference on Recent Advances in Concrete Technology, Washington D.C., USA, Sept. 2007, pp. 101–112.
[17] P. Sen, Time-dependent diffusion coefficient as a probe of geometry, Concepts Magn. Reson. A 23 (1) (2004) 1–21.
[18] L.L. Latour, R.L. Kleinberg, P.P. Mitra, C.H. Sotak, Pore-size distributions and tortuosity in heterogeneous porous media, J. Magn. Res. A 112 (1995) 83–91.
[19] N. Nestle, P. Galvosas, J. Kärger, Liquid-phase self-diffusion in hydrating cement pastes — results from NMR studies and perspectives for further research, Cem. Concr. Res. 37 (2007) 398–413.
[20] A. Atkinson, A.K. Nickerson, The diffusion of ions through water-saturated cement, J. Mater. Sci. 19 (1984) 3068–3078.
[21] E.J. Garboczi, D.P. Bentz, Computer simulation of the diffusivity of cement-based materials, J. Mater. Sci. 27 (1992) 2083–2092.
[22] K. Uesugi, Y. Suzuki, N. Yagi, A. Tsuchiyama, T. Nakano, Development of high spatial resolution X-ray CT system at BL47XU in SPring-8, Nucl. Instrum. Methods Phys. Res. A 467–468 (2001) 853–856.
[23] T. Nakano, A. Tsuchiyama, K. Uesugi, M. Uesugi, K. Shinohara, Slice -Software for basic 3-D analysis, Japan Synchrotron Radiation Research Institute (JASRI), 2006 <http://www-bl20.spring8.or.jp/slice/>.
[24] M.A.B. Promentilla, T. Sugiyama, T. Hitomi, N. Takeda, Studies on pore structure characterization in hydrated cement system based on 3D micro-geometry technique, Proceedings of the JCI symposium on Durability Mechanics, Tokyo, Japan, Dec. 2007.
[25] M. Koster, J. Hannawald, W. Brameshuber, Simulation of water permeability and water vapor diffusion through hardened cement paste, Comput. Mech. 37 (2) (2006) 163–172.
[26] J. Hoshen, R. Kopelman, Percolation and cluster distribution. I. Cluster multiple labeling technique and critical concentration algorithm, Phys. Rev., B 14 (8) (1976) 3438–3445.
[27] D. Stauffer, A. Aharony, Introduction to percolation theory, Revised 2nd ed.Taylor and Francis, London, 1994.
[28] S. Ikeda, N. Nakano, Y. Nakashima, Three-dimensional study on the interconnection and shape of crystals in a graphic granite by X-ray CT and image analysis, Mineral. Mag. 64 (5) (2000) 945–959.
[29] T. Ohkubo, Tortuosity based on anisotropic diffusion process in structured plate-like obstacles by Monte Carlo simulation, Transp. Porous Media 72 (2008) 339–350.
[30] T.C. Powers, T.L. Brownyard, Studies of the physical properties of hardened Portland cement pastes, Research Laboratories of the Portland Cement Association Bulletin, vol. 22 (1948), March 1948.
[31] R.A. Ketcham, W.D. Carlson, Acquisition, optimization, and interpretation of X-ray computed tomographic imagery: applications to the geosciences, Comput. Geosci. 27 (2001) 381–400.
[32] D.P. Bentz, E.J. Garboczi, Percolation of phases in a three-dimensional cement paste microstructural model, Cem. Concr. Res. 21 (1991) 325–344.
[33] E.J. Garboczi, D.P. Bentz, The effect of statistical fluctuation, finite size error, and digital resolution on the phase percolation and transport properties of the NIST cement hydration model, Cem. Concr. Res. 31 (10) (2001) 1501–1514.
[34] G. Ye, Percolation of capillary pores in hardening cement pastes, Cem. Concr. Res. 35 (2005) 167–176.
[35] P. Navi, C. Pignat, Simulation of cement hydration and the connectivity of capillary pore space, Adv. Cem. Based Mater. 4 (2) (1996) 58–67.
[36] C.H. Arns, M.A. Knackstedt, M.V. Pinczewski, W.B. Lindquist, Accurate estimation of transport properties from microtomographic images, Geophys. Res. Lett. 28 (17) (2001) 3361–3364.
[37] M.A. Knackstedt, C.H. Arns, T.J. Senden, K. Gross, Structure and properties of clinical coralline implants measured via 3D imaging and analysis, Biomaterials 27 (13) (2006) 2776–2786.
[38] T.C. Powers, L.E. Copeland, H.M. Mann, Capillary continuity or discontinuity in cement pastes, Portland Cem. Bull. 110 (1959) 3–12.
[39] A.J. Katz, A.H. Thompson, Quantitative prediction of permeability in porous rock, Phys. Rev., B 34 (1986) 8179–8181.
[40] E.J. Garboczi, Permeability, diffusivity, and microstructural parameters: a critical review, Cem. Concr. Res. 20 (1990) 591–601.
[41] P. Halamickova, R.J. Detwiler, D.P. Bentz, E.J. Garboczi, Water permeability and chloride ion diffusion in Portland cement mortars: relationship to sand content and critical pore diameter, Cem. Concr. Res. 25 (4) (1995) 790–802.